

Journal of Materials Chemistry A

Materials for energy and sustainability

Accepted Manuscript

This article can be cited before page numbers have been issued, to do this please use: K. Sotho, K. Kadota, T. Kurihara, T. Tiyawarakul, H. Yamada, K. Kongpatpanich and S. Horike, *J. Mater. Chem. A*, 2025, DOI: 10.1039/D4TA08744E.



This is an Accepted Manuscript, which has been through the Royal Society of Chemistry peer review process and has been accepted for publication.

Accepted Manuscripts are published online shortly after acceptance, before technical editing, formatting and proof reading. Using this free service, authors can make their results available to the community, in citable form, before we publish the edited article. We will replace this Accepted Manuscript with the edited and formatted Advance Article as soon as it is available.

You can find more information about Accepted Manuscripts in the [Information for Authors](#).

Please note that technical editing may introduce minor changes to the text and/or graphics, which may alter content. The journal's standard [Terms & Conditions](#) and the [Ethical guidelines](#) still apply. In no event shall the Royal Society of Chemistry be held responsible for any errors or omissions in this Accepted Manuscript or any consequences arising from the use of any information it contains.

ARTICLE

Conversion of CO₂ into Porous Metal-Organic Framework Monoliths

Kanchana Sotho,^a Kentaro Kadota,^{*b} Takuya Kurihara,^c Thanakorn Tiyyawarakul,^a Hiroki Yamada,^d Kanokwan Kongpatpanich,^a and Satoshi Horike^{*a,b,e}

We demonstrate one-pot conversion of CO₂ into amorphous formate-based metal-organic frameworks (MOFs) that form grain-boundary-free monoliths with permanent porosity through hot-pressing. The local coordination geometries of metal ions are characterized using solid-state NMR and synchrotron total X-ray scattering analyses. Hot-pressing decreases the pore sizes of monoliths, enhancing the adsorption selective toward H₂. The key for the formation of microporous monolith is the coordination network in which formate, capable of adopting various coordination modes, is connected via stable metal–oxygen bonds.

Received 00th January 20xx,
Accepted 00th January 20xx

DOI: 10.1039/x0xx00000x

1. Introduction

The conversion of CO₂ into functional materials is essential for realizing a carbon-neutral society.^{1–3} The synthesis of organic polymers and carbon materials from CO₂ as a feedstock has been extensively studied in the past few decades.^{4, 5} In recent years, the synthesis of metal-organic frameworks (MOFs) from CO₂ has gained attention.⁶ CO₂ is converted into bridging linkers, such as formate (OCHO[−]), formylhydroborate,⁷ carbamate,⁸ and carboxylate.⁹ On the other hand, the inherent inertness of CO₂ has restricted the structural diversity of CO₂-derived linkers and functionality of resultant MOFs. An approach to functionalize CO₂-derived MOFs that does not rely on the structural diversity of CO₂-derived linkers is highly demanded.

Tailoring structural disorder offers a powerful route for functionalizing solid materials. Amorphous materials, such as glasses and gels, lack long-range structural order and exhibit various features, e.g. defects, isotropy, transparency, and high mechanical strength.¹⁰ Amorphous MOFs exhibit unique functionalities that are not achieved by the crystalline analogues. For example, grain-boundary-free monoliths with

permanent porosity are formed via thermal and mechanical treatment, e.g. melt quench and hot-pressing.^{11, 12} The formability and processability of porous monoliths is attractive for enhanced volumetric gas storage capacity and recyclable heterogeneous catalysts.^{13, 14} Meanwhile, few studies focus on amorphous CO₂-derived MOFs and none of them show the formability of porous monoliths.^{7, 15}

In this work, we attempted to synthesize amorphous CO₂-derived MOFs showing permanent porosity as monolithic form. OCHO[−] was selected as a CO₂-derived bridging linker. Borohydride (BH₄[−]) readily converts CO₂ into OCHO[−] by hydride transfer.⁷ The small steric hindrance of OCHO[−] allows for various coordination geometries, making it suitable for constructing an isotropic grain-boundary-free structure.¹⁶ Oxophilic Al³⁺ and Ga³⁺ ions were employed to form a strong coordination bond with OCHO[−] that is essential to preserve a stable porous structure through hot-pressing treatment.¹⁷

2. Experimental section

2.1. Synthesis of OCHO[−]-based MOFs from CO₂

All chemicals were obtained from commercial suppliers and used without further purification. The powder samples of OCHO[−]-based MOFs denoted as **M-CO₂** (*M* = Al³⁺ and Ga³⁺), were synthesized from CO₂. Sodium borohydride (4.0 mmol) in anhydrous acetonitrile (MeCN, 20 mL) was reacted with CO₂ (99.99%) at 2.0 MPa at 25 °C for 1.5 hours in a high-pressure reaction vessel. The resulting suspension was mixed with metal nitrate salts (1.0 mmol) in anhydrous methanol (MeOH, 20 mL) at 100 °C for 48 hours. The white precipitate was isolated by centrifuge, washed with MeOH, and dried under vacuum (45 and 26% yields for **Al-CO₂** and **Ga-CO₂**).

^a Department of Materials Science and Engineering, School of Molecular Science and Engineering, Vidyasirimedhi Institute of Science and Technology, Rayong 21210, Thailand.

^b Department of Chemistry, Graduate School of Science, Kyoto University, Kitashirakawa-Oiwakecho, Sakyo-ku, Kyoto 606-8502, Japan.

^c Division of Material Chemistry, Graduate School of Natural Science and Technology, Kanazawa University, Kanazawa, Ishikawa 920-1192, Japan.

^d Diffraction and Scattering Division, Japan Synchrotron Radiation Research Institute (JASRI), Sayo, Hyogo 679-5198, Japan

^e Institute for Integrated Cell-Material Sciences, Institute for Advanced Study, Kyoto University, Yoshida-Honmachi, Sakyo-ku, Kyoto 606-8501, Japan.

Supplementary Information available: [details of any supplementary information available should be included here]. See DOI: 10.1039/x0xx00000x



2.2. General characterization

Thermogravimetric analysis (TGA) was carried out using a Rigaku Thermo plus TG 8122 under N₂ flow or air with a heating rate of 10 °C min⁻¹. Differential scanning calorimetry (DSC) was carried out by a Hitachi High-Tech DSC 7200 instrument under N₂ flow with a heating/cooling rate of 10 °C min⁻¹. Scanning electron microscope (SEM) and Energy-dispersive X-ray spectroscopy (EDX) was carried out using a JEOL JSM-7610F operated with an acceleration voltage of 200 kV. Transmission Electron Microscope and Energy-dispersive X-ray spectroscopy (TEM-EDS) was carried out using a JEOL JEM-ARM 200F. Fourier transform infrared (FT-IR) spectra were collected using a Bruker ALPHA II FT-IR spectrometer with a Universal ATR accessory under N₂ atmosphere. Inductively coupled plasma-optical emission spectrometry (ICP-OES) was carried out using an Agilent 700 series. The supernatant (200 µL) was dried and digested in a solution of 2% nitric acid with a total volume of 5 ml before a measurement. The average static water contact angle was measured at 25 °C, using a contact angle goniometer by dropping 10 µL of deionized water on three different locations on a monolith. The contact angle of the droplet was analyzed by the Ossila contact angle software.

2.3. X-ray analysis

Powder X-ray diffraction (PXRD) patterns were collected on a Rigaku SmartLab SE X-ray type with CuK α radiation ($\lambda = 1.54059$ Å). X-ray photoelectron spectrometer (XPS) spectra were collected using a JEOL XPS instrument (JPS-9010MC) with a Mg K α and Al K α source (1253.6 eV and 1486.6 eV) under high vacuum (10–7 Pa). All binding energy values were referenced to the C1s peak (284.70 eV). Synchrotron variable-temperature (VT) PXRD patterns were collected using synchrotron radiation ($\lambda = 0.99927$ Å) employing a large Debye-Scherrer camera with semiconductor detectors on the BL02B2 beamline at the Super Photon Ring (SPring-8, Hyogo, Japan). Pair distribution function (PDF) analysis was performed using synchrotron scattering data. Total X-ray scattering was collected at 30 °C with two 2D CdTe detectors at BL04B2 beamline in SPring-8. The incident energy was 112.9232 keV. $G(r)$ was obtained from the Fourier transform of $S(Q)$ with a Lorch modification function by using IgorPro software. X-ray absorption spectroscopy (XAS) including X-ray absorption near edge structure (XANES) and extended X-ray absorption fine structure (EXAFS) regions were performed in the transmission mode at BL14B2 beamline at SPring-8.

2.4. NMR analysis

¹H, ¹¹B, and ¹³C solution NMR spectra were collected using a Bruker Avance III HD 600 MHz. The powder samples were digested in 1.0 M DCl/D₂O/DMSO-*d*₆ for NMR measurement. CHN elemental analysis was performed using a LECO TruSpec Micro Element Series with cystine standard. Solid-state ¹H, ¹³C, and ²⁷Al magic-angle spinning (MAS) NMR experiments were conducted on a JEOL JNM-ECZ600R spectrometer at a 14.1 T superconductor magnet at room temperature. ¹³C cross-polarization (CP)/MAS, ¹H–¹³C 2D CP-heteronuclear correlation (HETCOR), ²⁷Al single-pulse, Hahn-echo, and 3QMAS

measurements were performed using a JEOL 3.2 mm double resonance MAS probe at a MAS rate of 20 kHz. In the CP/MAS sequence, a ¹H 90° pulse width of 2.3 µs and ¹H and ¹³C spin-lock pulse strengths of 70 and 50 kHz with a contact time of 3 ms were used. A ramped-amplitude spin-lock pulse was used for ¹³C. ¹³C signals were acquired under ¹H TPPM heteronuclear dipolar decoupling pulse irradiation with a pulse strength of 100 kHz. ²⁷Al single-pulse and Hahn-echo MAS spectra were measured with 90° and 180° pulse lengths of 1.15 and 2.3 µs. ²⁷Al 3QMAS spectrum was obtained using z-filter 3QMAS sequence. 0 quantum (Q)-3Q excitation, 3Q-0Q reconversion, and weak 90° pulse lengths of 3.3, 1.1, and 8.0 µs were used. ²⁷Al quadrupolar line-shape analysis was performed using ssNake software.¹⁸

2.5. Catalytic activity of *M*-CO₂ for CO₂ cycloaddition

Epichlorohydrin (ECH, 12.5 mmol), *M*-CO₂ (0.3–1.0 mol%), and tetrabutylammonium bromide (TBAB, 2.0 mol%) were added to the reaction vial (20 mL). CO₂ (99.99%) was introduced into the reaction mixture under stirring at 0.1 MPa at 30 °C for 48 hours. The reaction using styrene oxide was carried out at 80 °C. The conversion of ECH into chloropropylene carbonate (CPC) was calculated based on ¹H NMR analysis. The recovered catalyst was collected by centrifugation, followed by washing with fresh MeOH and dried in a vacuum.

2.6. Preparation of *M*-CO₂ monolith by hot-pressing

The powder sample of *M*-CO₂ (20 mg) was introduced into a 7-mm diameter stainless steel die set. A monolith was prepared under air by hot-pressing at 145 °C and 50–55 kN for 2 hours. After pressure release, the die set was taken out to cool down to room temperature.

2.7. Gas adsorption analysis

Gas adsorption isotherms were collected by MicrotracBEL BELSORP-mini X for N₂ at 77 K and CO₂ at 195, 273, and 298 K. Brunauer–Emmett–Teller surface areas (S_{BET}) were calculated from the N₂ adsorption isotherms. H₂ adsorption isotherms at 77 K were performed on MicrotracBEL BELSORP-mini II. The pore size distribution (PSD) was calculated using non-local density functional theory (NLDFT) method based on the N₂ adsorption isotherms. NH₃ temperature-programmed desorption (TPD) was carried out using a MicrotracBEL BELCAT. NH₃ was captured with 50 mg of powder sample at 40 °C for 30 minutes and the desorption profile was recorded by a TCD detector.

3. Results and discussion

3.1. Synthesis and structural characterizations of *M*-CO₂

The synthesis is a one-pot, two-step procedure involving the insertion of CO₂ into BH₄⁻ to afford formylhydroborate ([BH(OCHO)₃]⁻) and subsequent solvothermal reaction that converts [BH(OCHO)₃]⁻ into OCHO⁻ (Figure 1).⁷ This method is classified as a Type-II (one-pot) synthesis of CO₂-derived MOFs according to the literature.⁶ The choice of metal ions and solvents was essential for obtaining amorphous porous



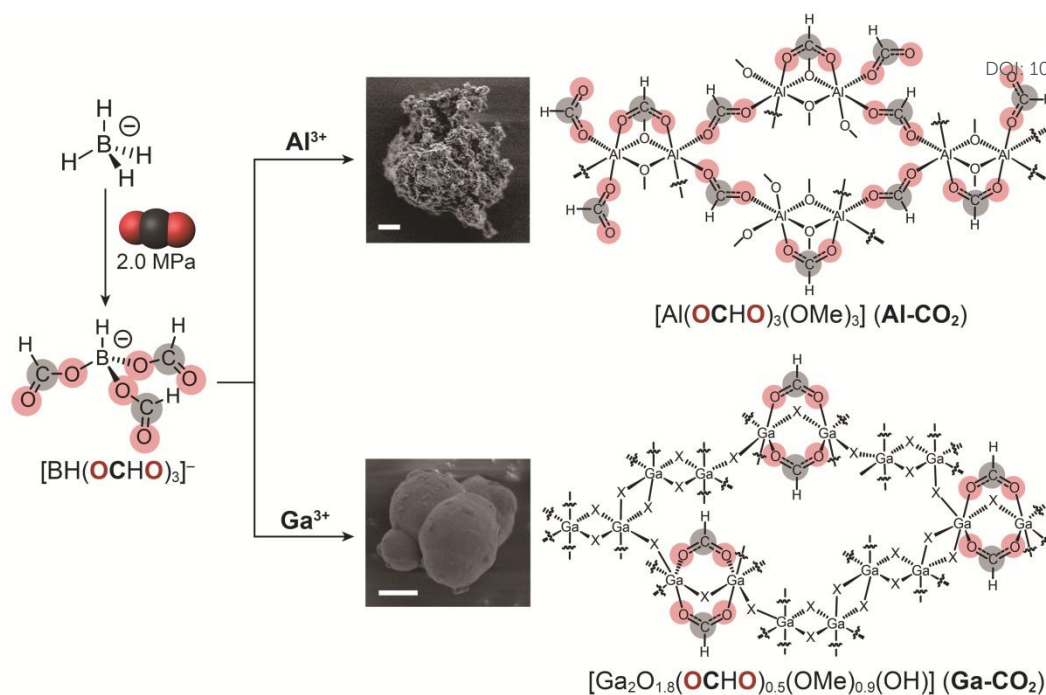


Figure 1. Schematic illustration of the synthesis and proposed structures of $M\text{-CO}_2$ ($M = \text{Al}^{3+}, \text{Ga}^{3+}$). Carbon and oxygen atoms derived from CO_2 are highlighted. The symbol X in the structure of Ga-CO_2 indicates either O^{2-} , OH^- , or OMe^- . SEM images of $M\text{-CO}_2$ are displayed, respectively. A scale bar indicates 1 μm .

structures. A synthetic attempt using Ce^{3+} ion instead of $\text{Al}^{3+}/\text{Ga}^{3+}$ resulted in a non-porous crystalline product (Figure S1-2). The larger ionic radius of Ce^{3+} led to a higher coordination number, forming a dense structure. Methoxide (MeO^-), derived from MeOH , serves as a linker in both $M\text{-CO}_2$ (details below). Control experiments using ethanol (EtOH) instead of MeOH as a synthetic solvent provided amorphous non-porous products consisting of OCHO^- and Al^{3+} without EtO^- (Figure S3-5). This indicates that the smaller steric hindrance of MeO^- is suitable for constructing the porous structure of $M\text{-CO}_2$.

Acid-digested solution NMR was carried out to confirm the formation of OCHO^- . The ^1H NMR spectra of $M\text{-CO}_2$ show peaks at 3.1 and 8.1 ppm corresponding to MeO^- and OCHO^- , respectively. The ratios of OCHO^- and MeO^- were calculated as 1:1 and 1:1.8 for Al-CO_2 and Ga-CO_2 (Figure S6). The assignment was also confirmed by ^{13}C NMR (Figure S7). The ^{11}B NMR spectra showed that $M\text{-CO}_2$ contained no boron species derived from NaBH_4 (Figure S8). The FT-IR spectra exhibit the $\text{C}=\text{O}$ stretching vibration of OCHO^- were observed at 1581 and 1652 cm^{-1} for Al-CO_2 and Ga-CO_2 , respectively (Figure S9).¹⁹ A broad peak at 3420 cm^{-1} in Ga-CO_2 was attributed to the O-H stretching vibration of OH^- .²⁰

The metal content of $M\text{-CO}_2$ was determined by pyrolysis under air. TGA heating up to 900 $^\circ\text{C}$ under a flow of air fully converted $M\text{-CO}_2$ into corresponding metal oxides (Figure S10-11). The gravimetric metal contents were calculated as 19.3 and 59.1 wt% for Al-CO_2 and Ga-CO_2 , respectively. Given the results of CHN elemental analysis, the chemical compositions were determined as $[\text{Al}_2(\text{OCHO})_3(\text{OMe})_3]$ for Al-CO_2 and $[\text{Ga}_2\text{O}_{1.8}(\text{OCHO})_{0.5}(\text{OMe})_{0.9}(\text{OH})]$ for Ga-CO_2 . The gravimetric

CO_2 content was calculated as 46.8 and 9.3 wt% for Al-CO_2 and Ga-CO_2 (Table S1).

The PXRD patterns exhibit broad features at 8.1, 10.8, and 12.3 $^\circ$ for Al-CO_2 and at 5.1 $^\circ$ for Ga-CO_2 , which do not match the reported patterns of metal formate compounds (Figure 2A and S12).^{19, 21, 22} SEM-EDX exhibits spherical particles with a diameter of 5 and 2 μm for Al-CO_2 and Ga-CO_2 respectively and a homogeneous distribution of each metal element (Figure 1 and S13-14). TEM-EDS confirmed also confirmed homogeneous distribution of each element in $M\text{-CO}_2$ (Figure S15-16). Solid-state $^1\text{H}\text{-}^{13}\text{C}$ CP-HETCOR NMR experiment was carried out to examine the intermolecular distance correlation between OCHO^- and MeO^- . The $^1\text{H}\text{-}^{13}\text{C}$ HETCOR NMR spectrum of Al-CO_2 exhibits a clear correlation peak between ^1H of OCHO^- at 8.5 ppm and ^{13}C of MeO^- at 51.5 ppm (Figure 2B). Ga-CO_2 also exhibits the correlation between OCHO^- and MeO^- (Figure S17). The observed correlations indicate both OCHO^- and MeO^- are homogeneously distributed to form the structure of $M\text{-CO}_2$.

The local coordination geometry of Al^{3+} was characterized by ^{27}Al MAS NMR. The ^{27}Al NMR spectrum of Al-CO_2 exhibits an asymmetric line shape due to the ^{27}Al quadrupolar interaction (Figure S18). To analyze the coordination structure, we performed quadrupolar line-shape fitting to the ^{27}Al 1D spectrum sliced at the peak center of the isotropic dimension (12.31 ppm) of the 3QMAS spectrum (Figure 2C and S19). The isotropic chemical shift $\delta_{\text{iso}} = 8.21$ ppm, quadrupolar coupling constant $C_Q = 5.00$ MHz, and asymmetry parameter $\eta = 0.48$ were obtained. The δ_{iso} value suggests that Al^{3+} forms an octahedral six-coordinated geometry.^{23, 24} The ^{27}Al MAS spectrum of $[\text{Al}(\text{OCHO})_3]$, possessing the highly symmetric $\text{Al}^{3+}\text{-}6\text{O}$ coordination structure, shows a narrow peak with $C_Q \sim 0$



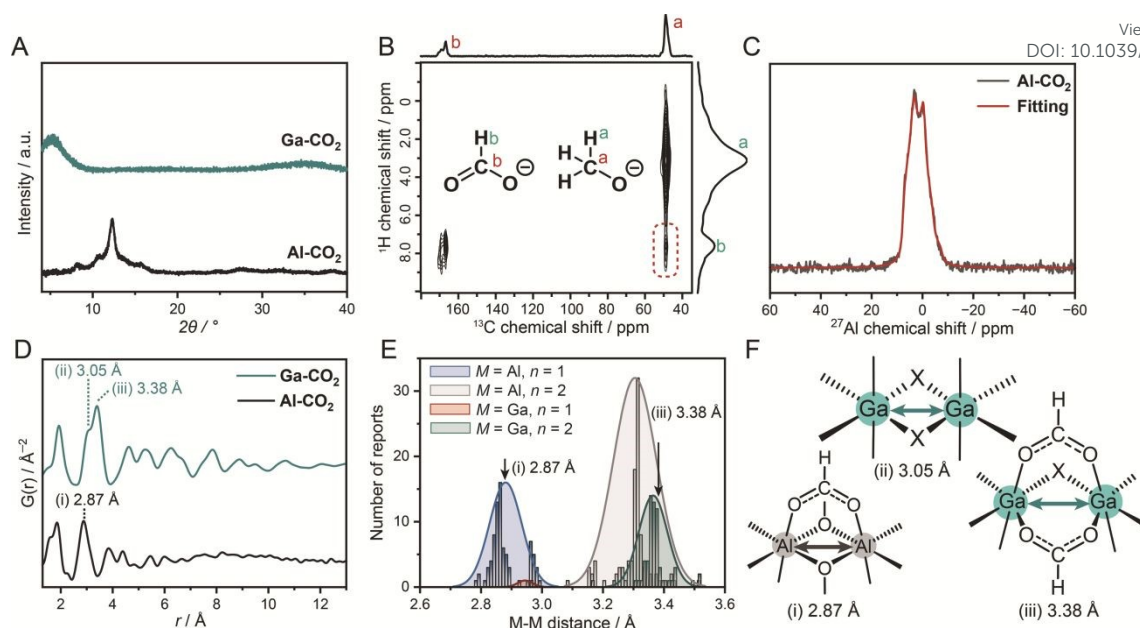
View Article Online
DOI: 10.1039/D4TA08744E

Figure 2. Structural characterizations of $M\text{-CO}_2$. (A) PXRD patterns of Al-CO_2 and Ga-CO_2 . (B) ^1H - ^{13}C CP-HETCOR NMR spectra of Al-CO_2 . A correlation between ^1H of OCHO^- and ^{13}C of MeO^- is highlighted as a green box. (C) ^{27}Al 1D sliced 3QMAS NMR spectrum (black) and fitting (red) of Al-CO_2 . (D) PDF profiles of Al-CO_2 and Ga-CO_2 . (E) Histograms of M-M distances for $[M-(R\text{-COO})_n(X)_{3-n}\text{-}M]$ with Gaussian distribution. (F) Proposed M-M building units of $M\text{-CO}_2$. $X = \text{O}^{2-}$, OH^- , or OMe^- .

(Figure S20). The larger C_Q value of Al-CO_2 reflects an asymmetric coordination structure of Al^{3+} bound with both OCHO^- and MeO^- . The non-zero η suggests a low axial-symmetry structure around Al^{3+} due to the random distribution of the two linkers. The coordination geometry of Ga^{3+} in Ga-CO_2 was characterized by synchrotron XAS. The EXAFS fitting on the first coordination shell confirmed that the coordination number of Ga^{3+} in Ga-CO_2 was 5.6 ± 0.6 , which is indicative of octahedral geometry (Figure S21 and Table S2). The formation of octahedral geometry in $M\text{-CO}_2$ was also confirmed by XPS (Figures S22-23). The binding energy of O (1s), C (1s), and Al ($2p_{3/2}$) show at 530.1, 288.0 and 71.6 eV in Al-CO_2 which correspond to Al-O coordination and the presence of OHCO^- .²⁵ Ga-CO_2 shows binding energy of O (1s) and Ga ($2p_{3/2}$) at 531.5 eV and 1118.9 eV which belong to Ga-O bond and Ga^{3+} , respectively.

PDF analysis was performed to characterize the structural periodicity of $M\text{-CO}_2$ (Figure 2D). The peaks below 2 Å were assigned as the metal-oxygen bonds (1.85 and 1.95 Å for Al-CO_2 and Ga-CO_2).^{26, 27} The peaks between 2.0 and 4.0 Å are assigned as metal-metal (M-M) correlations (2.87 Å for Al-CO_2 and 3.05 and 3.38 Å for Ga-CO_2). To figure out the bridging mode of M-M, we surveyed M-M distances of an $\text{Al}^{3+}/\text{Ga}^{3+}$ -based coordination compound with octahedral geometry and $R\text{-COO}^-$ groups in the CCDC database. The histograms of M-M distances were plotted for the building units of $[M-(R\text{-COO})_n(X)_{3-n}\text{-}M]$ ($M = \text{Al}^{3+}$, Ga^{3+} ; $X = \text{O}^{2-}/\text{OH}^-/\text{OMe}^-$; $n = 1, 2$, Figure 2E). We assign the peak at 2.87 Å in Al-CO_2 as $[\text{Al}(\text{OCHO})(\text{OMe})_2\text{-Al}]$ and 3.38 Å in Ga-CO_2 as $[\text{Ga}(\text{OCHO})_2(X)\text{-Ga}]$ (Figure 2E). The peak at 3.05 Å in Ga-CO_2 is assigned as $[\text{Ga}(X)_2\text{-Ga}]$, edge-sharing octahedral geometry (Figure 2F, Table S3-4). The mixed coordination of OCHO^- and OMe^- in Al-CO_2 is consistent with the low axial-

symmetry structure of Al^{3+} observed by ^{27}Al MAS NMR. The longer-range periodicity was observed up to around 8 and 12 Å for Al-CO_2 and Ga-CO_2 . The extended network is formed by connecting the M-M building units as proposed in Figure 1.

3.2. Thermal and chemical stability

The TGA profiles under N_2 indicate that no significant weight loss was up to 190 and 180 °C for Al-CO_2 and Ga-CO_2 (Figure S24). The thermal stability is slightly lower than those of $[\text{M}(\text{OCHO})_3]$ (decomposition temperatures: 200 and 230 °C for Al^{3+} and Ga^{3+}).²¹ The thermal stability of Al-CO_2 was studied by synchrotron variable-temperature PXRD (Figure S25). The crystallinity of Al-CO_2 was maintained up to 200 °C and the intensity reduced when heated to 320 °C. The stability of common organic solvents was also studied. The PXRD pattern of Al-CO_2 was intact after soaking in common organic solvents, e.g. tetrahydrofuran, chloroform, and toluene, for 24 h at 25 °C, respectively (Figure S26).

3.3. Characterization of defective open metal site (OMS) for CO_2 cycloaddition

We evaluated the Lewis acidity of defective OMS in $M\text{-CO}_2$ by NH_3 -TPD (Figure 3). NH_3 was completely released below 190 °C within 2 hours, indicating the defective OMS in $M\text{-CO}_2$ are classified as weak acid sites.²⁸ The total acidic sites were calculated as 0.59 and 2.25 mmol g^{-1} for Al-CO_2 and Ga-CO_2 , respectively. The larger amount of acidic sites in Ga-CO_2 was attributed to a defective OMS in the amorphous structure.¹⁵ Defective OMS serves as a catalytically active site for CO_2 cycloaddition with epoxides. The catalytic activity of $M\text{-CO}_2$ was evaluated with ECH as a model reaction. The solvent-free reaction of ECH and CO_2 with the presence of 1.0 mol% of $M\text{-CO}_2$ and TBAB as a co-catalyst at 30 °C yielded CPC with high



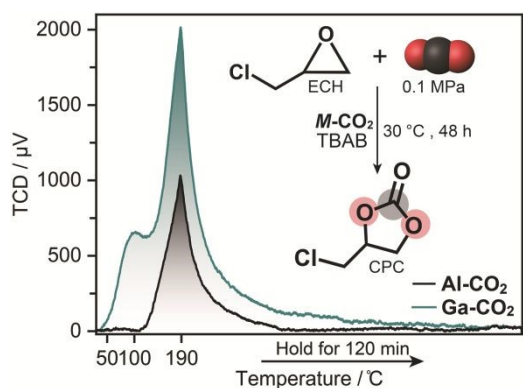


Figure 3. NH_3 -TPD profiles of M-CO_2 . Inset: conversion of ECH into CPC via CO_2 cycloaddition reaction using M-CO_2 catalysis with TBAB as a co-catalyst.

conversion of 94.4 and 91.6% for Al-CO_2 and Ga-CO_2 (Figure 3 and S27). The catalyst amount and reaction time were optimized in the range of 0.3–1.0 mol% and 12–72 h (Figure S28 and Table S5). The control experiment using only TBAB without M-CO_2 catalysts resulted in a conversion of 67.5%. The catalytic activity of M-CO_2 maintained the conversion exceeding 90% after three cycles, which is comparable to those of MOFs with catalytically active OMS (Table S7).^{29–31} ICP-OES on the supernatant after the reactions confirms negligible leaching of metal ions from M-CO_2 over three cycles (Al-CO_2 : 0.14–0.33 ppm and Ga-CO_2 : 0.07 ppm, Table S7).^{32, 33} Al-CO_2 also exhibited

catalytic activity toward the CO_2 cycloaddition of styrene oxide into styrene carbonate at 80 °C with conversion of 76.3% (Figure S29 and Table S6). Although the diffraction intensity of recycled Al-CO_2 decreased in PXRD, N_2 adsorption isotherms and S_{BET} values were comparable after three cycles (Figure S30–31). In contrast, the recycled Ga-CO_2 exhibited a large decrease in N_2 adsorption, whereas the catalytic activity was preserved. This indicates the catalytic reaction in Ga-CO_2 mainly occurred at the particle surface rather than internal pores, which is consistent with the catalytic CO_2 cycloaddition at the surface of dense MOFs.³⁴ This is also supported by the smaller pore size of Ga-CO_2 than Al-CO_2 confirmed by N_2 adsorption (Figure S32). The results indicate that CO_2 -derived MOFs serve as a catalyst for CO_2 cycloaddition at ambient conditions.

3.4. Formability of transparent monoliths

Hot-pressing provided a transparent monolith of Al-CO_2 (Figure 4A). In contrast, the Ga-CO_2 monolith prepared by hot-pressing in the same condition was not transparent. The PXRD pattern of the Al-CO_2 monolith exhibits broad features in the same peak positions before hot-pressing, indicative of preservation of the long-range order (Figure S33). The differential scanning calorimetry (DSC) profile of Al-CO_2 ground powder does not display any features assignable to the glass transition in the temperature range from –50 to 150 °C (Figure S34). The SEM image of the Al-CO_2 monolith displays a grain-boundary-free, smooth surface, resulting in the formation of a transparent monolith (Figure 4B and S35). The surface hydrophobicity of the

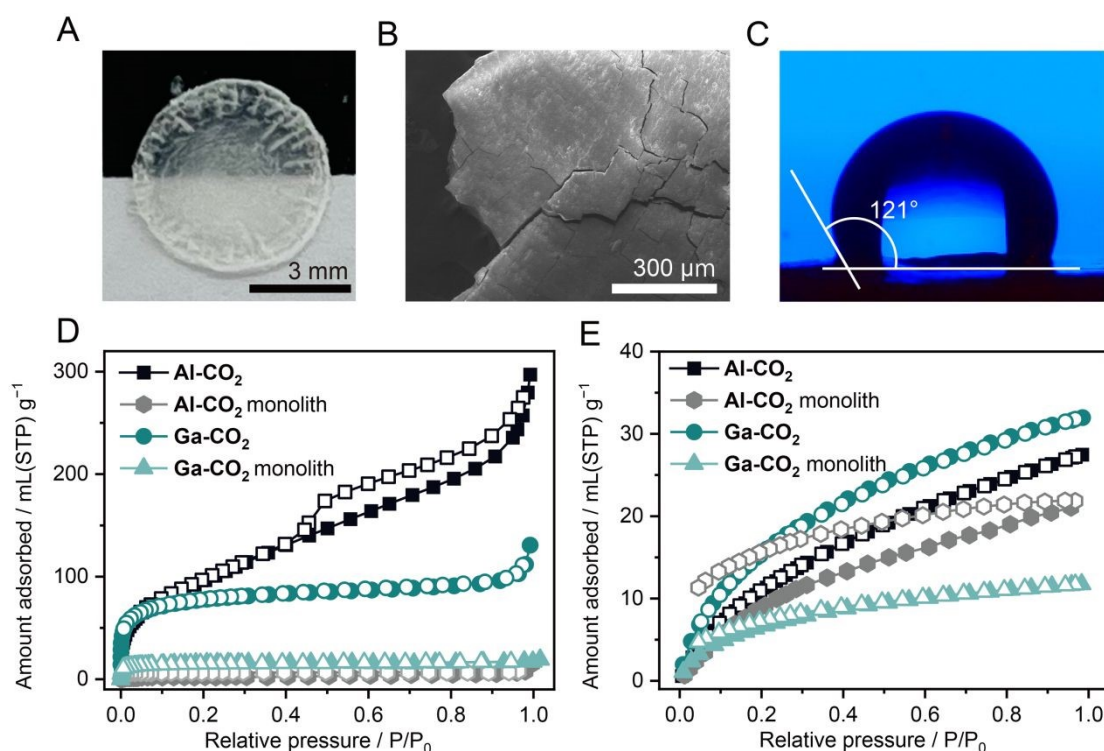


Figure 4. (A) Optical image of transparent Al-CO_2 monolith with a diameter of 7.0 mm. (B) SEM image of Al-CO_2 monolith. (C) Image of water droplet on the surface of Al-CO_2 monolith. (D) N_2 and (E) H_2 adsorption isotherms at 77 K for M-CO_2 powder and monoliths. Solid/open symbols indicate adsorption/desorption isotherms, respectively.



M-CO₂ monolith was tested by a contact angle analysis (Figure 4C and S36). The monolithic samples of **Al-CO₂** and **Ga-CO₂** exhibit water contact angles of 121 ± 0.4 and $116 \pm 0.8^\circ$, which is categorized as a hydrophobic surface as the angles greater than 90° .³⁵ The hydrophobic feature of **M-CO₂** is attributed to the presence of methyl group of MeO⁻. The lower hydrophobicity of **Ga-CO₂** was due to the OH⁻ group which can form hydrogen bonding with water molecules.³⁵

3.5. Porous properties as powder and monoliths

The porous properties of MOFs as a monolithic form are also essential for wide applications such as catalytic processes and volumetric gas adsorption capacity.³⁶⁻³⁸ The gas adsorption measurements were carried out for both powder and monolith samples (N₂ at 77 K, CO₂ at 195 K, and H₂ at 77 K, Figure 4D, 4E and S37). The gas uptake and *S*_{BET} values calculated from the N₂ adsorption isotherms are displayed (Table S8). The N₂ and CO₂ uptake of **M-CO₂** monoliths largely decreased by 94 and 81 % for **Al-CO₂** and 85 and 83 % for **Ga-CO₂**, respectively (Table S8). This is consistent with the decrease of *S*_{BET} values of **M-CO₂** monoliths, which is reduced by 91% for **Al-CO₂** and 80% for **Ga-CO₂**. In contrast, **M-CO₂** monoliths exhibit a smaller decrease in H₂ uptake compared to the reduction in N₂ and CO₂ uptake (22 and 63% for **Al-CO₂** and **Ga-CO₂**, respectively). As the kinetic diameters increase (2.89, 3.30, and 3.65 Å for H₂, CO₂, and N₂),³⁹ the larger decreases in gas uptake for both **M-CO₂** monoliths were observed. This indicates the pore size reduction of **M-CO₂** through hot-pressing, which is consistent with mechanical pressure-induced pore size reduction observed in flexible zeolitic imidazolate frameworks (ZIFs).⁴⁰ The key for the preservation of microporosity of **M-CO₂** as monolithic form is attributed to the coordination network in which OCHO⁻, capable of adopting various coordination modes, is connected via stable Al/Ga–O bonds. Hybrid perovskites composed OCHO⁻ exhibit structural transformation in response to mechanical pressure, driven by alternation in the coordination modes of OCHO⁻.⁴¹ The flexibility of the coordination geometry of OCHO⁻ is originating from its low steric hindrance.¹⁶ Due to the coordination flexibility and stable Al/Ga–O bonds, hot-pressing does not collapse **M-CO₂** into a non-porous structure, and the microporous structure is maintained while the pore size decreases.

4. Conclusions

We demonstrated the one-pot synthesis of amorphous MOFs with permanent porosity, [Al₂(OCHO)₃(OMe)₃] (**Al-CO₂**) and [Ga₂O_{1.8}(OHCO)_{0.5}(OMe)_{0.9}(OH)] (**Ga-CO₂**), from CO₂ by converting CO₂ into OHCO⁻. The local coordination geometries of metal center were revealed by solid-state NMR and synchrotron total X-ray scattering analysis. **Al-CO₂** formed a grain-boundary-free transparent microporous monolith via hot-pressing. Hot-pressing treatment mechanically reduced the pore size of **M-CO₂** monoliths, enhancing adsorption selectivity toward H₂. The key for the formation of porous monolith was attributed to the coordination flexibility of OHCO⁻ and stable metal-oxygen bonds. These findings offer a new design

guideline for CO₂-derived porous materials by incorporating structural disorder.

DOI: 10.1039/D4TA08744E

Author contributions

K.K., S.H. and K.S. designed the project. K.S., K.K., T.K., T.T., H.Y., and K.K. contributed to data collection and formal analyses. K.K., S.H. and K.S. wrote the manuscript and all the authors approved the final version.

Conflicts of interest

There are no conflicts to declare.

Data availability

The data supporting this article have been included as part of the ESI.†

Acknowledgments

This work was supported by the Japan Society of the Promotion of Science (JSPS) for a Grant-in-Aid for Early-Career Scientists (JP24K17696), Transformative Research Areas (A) "Supraceramics" (JP22H05147), Fund for the Promotion of Joint International Research (Inter-national Collaborative Research, JP24K0112) from the Ministry of Education, Culture, Sports, Science and Technology (MEXT), Japan, and Thailand Science Research and Innovation (TSRI) under the fiscal year 2025 funding program (FRB680014/0457NM). The synchrotron radiation experiments were performed at BL02B2, BL04B2, and BL14B2 in SPring-8 with the approval of RIKEN (2023B1639, 2023B1721, and 2023B2001).

Notes and references

1. J. Artz, T. E. Muller, K. Thenert, J. Kleinekorte, R. Meys, A. Sternberg, A. Bardow and W. Leitner, *Chem. Rev.*, 2018, **118**, 434-504.
2. A. Otto, T. Grube, S. Schiebahn and D. Stolten, *Energy Environ. Sci.*, 2015, **8**, 3283-3297.
3. Q. Liu, L. Wu, R. Jackstell and M. Beller, *Nat. Commun.*, 2015, **6**, 5933.
4. X. Cheng, M. Wu, J. Li, W. Wang, N. Mitsuzaki and Z. Chen, *Catal. Sci. Technol.*, 2023, **13**, 3891-3900.
5. B. Grignard, S. Gennen, C. Jerome, A. W. Kleij and C. Detrembleur, *Chem. Soc. Rev.*, 2019, **48**, 4466-4514.
6. K. Kadota and S. Horike, *Acc. Chem. Res.*, 2024, **57**, 3206-3216.
7. K. Kadota, N. T. Duong, Y. Nishiyama, E. Sivaniah and S. Horike, *Chem. Commun.*, 2019, **55**, 9283-9286.
8. K. Kadota, Y. L. Hong, Y. Nishiyama, E. Sivaniah, D. Packwood and S. Horike, *J. Am. Chem. Soc.*, 2021, **143**, 16750-16757.
9. B. Song, Y. Liang, Y. Zhou, L. Zhang, H. Li, N.-X. Zhu, B. Z. Tang, D. Zhao and B. Liu, *J. Am. Chem. Soc.*, 2024, **146**, 14835-14843.



10. Z. Guo, Z. Liu and R. Tang, *Mater. Chem. Front.*, 2024, **8**, 1703-1730.
11. Y. Zhao, S. Y. Lee, N. Becknell, O. M. Yaghi and C. A. Angell, *J. Am. Chem. Soc.*, 2016, **138**, 10818-10821.
12. Y.-S. Wei, Z. Fan, C. Luo and S. Horike, *Nat. Synth.*, 2023, **3**, 214-223.
13. J. Hou, A. F. Sapnik and T. D. Bennett, *Chem. Sci.*, 2020, **11**, 310-323.
14. D. G. Madden, D. O'Nolan, N. Rampal, R. Babu, C. Camur, A. N. Al Shakh, S. Y. Zhang, G. A. Rance, J. Perez, N. P. Maria Casati, C. Cuadrado-Collados, D. O'Sullivan, N. P. Rice, T. Gennett, P. Parilla, S. Shulda, K. E. Hurst, V. Stavila, M. D. Allendorf, J. Silvestre-Albero, A. C. Forse, N. R. Champness, K. W. Chapman and D. Fairen-Jimenez, *J. Am. Chem. Soc.*, 2022, **144**, 13729-13739.
15. Z. Fang, Y. Hu, B. Yao, Z. Z. Ye and X. S. Peng, *J. Mater. Chem. A*, 2024, **12**, 6112-6122.
16. A. D. Nicholas, A. Arteaga, L. C. Ducati, E. C. Buck, J. Autschbach and R. G. Surbella III, *Chem. Eur. J.*, 2023, **29**, e202300077.
17. W. Xu, N. Hanikel, K. A. Lomachenko, C. Atzori, A. Lund, H. Lyu, Z. Zhou, C. A. Angell and O. M. Yaghi, *Angew. Chem. Int. Ed.*, 2023, **62**, e202300003.
18. S. G. J. van Meerten, W. M. J. Franssen and A. P. M. Kentgens, *J. Magn. Reson.*, 2019, **301**, 56-66.
19. V. N. Krasil'nikov, A. P. Tyutyunnik, I. V. Baklanova, A. N. Enyashin, I. F. Berger and V. G. Zubkov, *CrystEngComm*, 2018, **20**, 2741-2748.
20. M. Calatayud, S. E. Collins, M. A. Baltanás and A. L. Bonivardi, *Phys. Chem. Chem. Phys.*, 2009, **11**, 1397-1405.
21. Y.-Q. Tian, Y.-M. Zhao, H.-J. Xu and C.-Y. Chi, *Inorg. Chem.*, 2007, **46**, 1612-1616.
22. K. Kadota, N. T. Duong, Y. Nishiyama, E. Sivaniah and S. Horike, *Chem. Commun.*, 2019, **55**, 9283-9286.
23. S.-Y. Yang, Y. Yan, B. Lothenbach and J. Skibsted, *J. Phys. Chem. C*, 2021, **125**, 27975-27995.
24. M. Haouas, F. Taulelle and C. Martineau, *Prog. Nucl. Magn. Reson. Spectrosc.*, 2016, **94-95**, 11-36.
25. T. Song, Q. Liu, J. Liu, W. Yang, R. Chen, X. Jing, K. Takahashi and J. Wang, *Appl. Surf. Sci.*, 2015, **355**, 495-501.
26. J. A. van Bokhoven, A. M. J. van der Eerden and D. C. Koningsberger, *J. Am. Chem. Soc.*, 2003, **125**, 7435-7442.
27. P. Castro-Fernández, M. V. Blanco, R. Verel, E. Willinger, A. Fedorov, P. M. Abdala and C. R. Müller, *J. Phys. Chem. C*, 2020, **124**, 20578-20588.
28. A. Eskemech, H. Chand, A. Karmakar, V. Krishnan and R. R. Koner, *Inorg. Chem.*, 2024, **63**, 3757-3768.
29. P.-Z. Li, X.-J. Wang, J. Liu, J. S. Lim, R. Zou and Y. Zhao, *J. Am. Chem. Soc.*, 2016, **138**, 2142-2145.
30. X.-Y. Li, L.-N. Ma, Y. Liu, L. Hou, Y.-Y. Wang and Z. Zhu, *ACS Appl. Mater. Interfaces.*, 2018, **10**, 10965-10973.
31. G. Zhang, G. Wei, Z. Liu, S. R. J. Oliver and H. Fei, *Chem. Mater.*, 2016, **28**, 6276-6281.
32. S. Kaewsai, S. Del Gobbo and V. D'Elia, *ChemCatChem*, 2024, **16**, e202301713.
33. C. Chen, J. Zhang, G. Li, P. Shen, H. Jin and N. Zhang, *Dalton Trans.*, 2014, **43**, 13965-13971.
34. J. L. Obeso, J. G. Flores, C. V. Flores, V. B. Lopez-Cervantes, V. Martinez-Jimenez, J. A. de Los Reyes, E. Lima, D. Solis-Ibarra, I. A. Ibarra, C. Leyva and R. A. Peralta, *Dalton Trans.*, 2023, **52**, 12490-12495.
35. L.-H. Xie, M.-M. Xu, X.-M. Liu, M.-J. Zhao and J.-R. Li, *Adv. Sci.*, 2020, **7**, 1901758. DOI: 10.1039/D4TA08744E
36. B. Yeskendir, J.-P. Dacquin, Y. Lorguilloux, C. Courtois, S. Royer and J. Dhainaut, *Mater. Adv.*, 2021, **2**, 7139-7186.
37. M. I. Nandasiri, S. R. Jambovane, B. P. McGrail, H. T. Schaefer and S. K. Nune, *Coord. Chem. Rev.*, 2016, **311**, 38-52.
38. S. Vaidya, O. Veselska, A. Zhadan, M. Diaz-Lopez, Y. Joly, P. Bordet, N. Guillou, C. Dujardin, G. Ledoux, F. Toche, R. Chiriac, A. Fateeva, S. Horike and A. Demessence, *Chem. Sci.*, 2020, **11**, 6815-6823.
39. G. Zheng, J. Wu, Y. Jia, G. Han and S. Zhang, *J. Membr. Sci.*, 2024, **705**, 122924.
40. S. Henke, M. T. Wharmby, G. Kieslich, I. Hante, A. Schneemann, Y. Wu, D. Daisenberger and A. K. Cheetham, *Chem Sci*, 2018, **9**, 1654-1660.
41. S. Sobczak and A. Katrusiak, *Inorg. Chem.*, 2019, **58**, 11773-11781.

